FEATURE ARTICLE

Check for updates

Frontiers in ^{19}F-MR imaging: nanofluorides and ^{19}F-CEST as novel extensions to the ^{19}F-MRI toolbox

Andrea Galisova (ID) [ab] and Amnon Bar-Shir (ID) *[a]

Fluorine-containing materials have enriched the field of molecular and cellular MRI with unambiguous and quantitative detection capabilities. The background-free "hot-spot" display and the large range of chemical shifts of the broad palette of ^{19}F-formulations are now used for a variety of applications. The common features of these formulations are: (i) they are based on organic molecular backbones (*i.e.*, organofluorines); and (ii) their ^{19}F-MRI detectability relies on a well-defined and clearly observed ^{19}F-MR signal. During the last few years, our lab aimed to expand the ^{19}F-MR toolbox with new capabilities that were, thus far, not used in molecular and cellular ^{19}F-MRI. This Feature Article summarizes our developments and implementations in the field of ^{19}F-MRI emphasizing (i) the introduction of ultrasmall inorganic fluoride-based nanocrystals (nanofluorides) as nano-sized (<10 nm) agents for ^{19}F-MRI, and (ii) the use of Chemical Exchange Saturation Transfer (CEST) in the ^{19}F-MRI framework to indirectly amplify ^{19}F-MR signals of otherwise-undetected fluorinated entities.

[a] *Department of Molecular Chemistry and Materials Science, Weizmann Institute of Science, Herzl Street 234, Rehovot, Israel. E-mail: amnon.barshir@weizmann.ac.il*
[b] *Institute for Clinical and Experimental Medicine, Videnska 1958/9, Prague, Czech Republic*

Andrea Galisova

Andrea Galisova completed her PhD at Charles University in Prague in 2018 under the supervision of Assoc. Prof. Daniel Jirak. Her thesis explored the use of contrast agents for labeling of transplanted cells intended for ^{1}H/^{19}F-MRI visualization (CEST agents, perfluorocarbons, and small molecules). Afterward, she joined the group of Prof. Amnon Bar-Shir at the Weizmann Institute of Science in Israel for a postdoctoral stay, where she worked on ^{19}F-MRI of nanofluorides and MRI visualization of genetically-engineered extracellular vesicles. Since 2022, she has been working at the Institute for Clinical and Experimental Medicine in Prague on the development of (extra)cellular molecular probes for heteronuclear MR imaging.

Amnon Bar-Shir

Amnon Bar-Shir is an Associate Professor at the Weizmann Institute of Science, Rehovot Israel. Amnon earned his BSc (2002) and MSc (2004, under Michael Gozin), and PhD (2009, under Yoram Cohen) from Tel Aviv University. As a postdoc at the Johns Hopkins University School of Medicine under Assaf Gilad he developed genetically engineered reporters for MRI. In 2014 he joined the Weizmann Institute, where his lab uses synthetic chemistry, nanofabrication, and protein engineering to generate novel molecular formulations, such as small molecules, nanocrystals, supramolecular assemblies, and proteins, as MRI sensors of high sensitivity, specificity, and orthogonality. Prof. Bar-Shir won multiple research grants, including the ERC starting grant (ERC-StG 2015) and the ERC consolidator grant (ERC-CoG 2022). He was recognized with several awards including the 2014 NIH Pathway to Independence Award, the 2019 Krill Prize, and the 2021 ICS Excellent Young Scientist Prize.

Introduction

From the early days of magnetic resonance imaging (MRI), fluorine-19-containing materials have attracted much interest due to their favorable MR properties, which has led to the revolution of the field of ^{19}F-MRI, featuring several advantages over ^{1}H-MRI.[1] The very similar sensitivity of ^{19}F-MR (ca. 83%) to that of ^{1}H-MR, the need for only minimal hardware adjustments, and the negligible amounts of ^{19}F-content in soft tissues all make fluorinated compounds very attractive for molecular and cellular MRI applications. The unambiguous and quantitative detection capabilities of ^{19}F-rich materials provide ^{19}F-MRI with "background-free" readouts that are frequently presented as "hot spots" over high-resolution ^{1}H-MRI maps that represent anatomical views of the same studied subject. In addition, the very wide range of ^{19}F-NMR chemical shifts, which span over 350 ppm, enables the mapping of multiple fluorinated probes simultaneously and the display of these probes as artificial MRI "colors" for multi-target imaging purposes.

Throughout the years, with the development of the field of molecular and cellular MR imaging, and, in parallel to the extensive progress in the design and implementation of both paramagnetic and super-paramagnetic agents for a wide range of applications, ^{19}F-agents became appealing. In that regard, numerous types of ^{19}F-probes were developed, including small molecules,[2,3] metal complexes,[4,5] and macromolecules and polymers.[6,7] Widely used and clinically applied perfluorocarbons (PFCs)[8] with a high fluorine-19 content have revolutionized ^{19}F-MR research, leading to broad applications in cellular imaging.[9–17] In addition to the ^{19}F-MR signal, several probes offer targetability toward specific molecular signatures of pathological tissues, such as entities displayed on the surface of cancer cells or acidic pH and the altered redox environment in tumors,[18–20] enabling precise diagnosis, and therefore, accurate therapy of diseases.[21,22] Activatable ^{19}F-MRI probes that respond to various types of stimuli were designed. For example,

activable probes to sense metal ions,[23] e.g. Zn^{2+},[24] Cu^{2+},[25] Mn^{2+}[26] and enzymes,[2,27] or to detect alterations in the local environment, such as redox,[7,28,29] pH,[30–32] and temperature,[33,34] via changes in the ^{19}F-MR signal. Due to their signal specificity, stimuli-triggered probes have a wide range of applications and are particularly useful for quantifying parameters that influence their response.

The growth of fluorinated molecular probes and their applications in ^{19}F-MRI continues and many of the developments are beyond the scope of this Feature Article and can be found in other reviews.[35–39] Interestingly, although there are diverse types of probes, the vast majority (if not all) of the used ^{19}F-probes developed and used are based on organofluorines with a centered carbon–fluorine bond, with no demonstration of the inorganic fluoride-based formulations used for ^{19}F-MRI. In addition, the MRI signals of these organofluorine formulations rely on the ability to directly detect their well-defined ^{19}F-MR readout at a specific resonance frequency. This prevents ^{19}F-MRI from being used to study very low concentrations of biological targets—those which can be found at levels that cannot be detected just by applying a stronger magnetic field or increasing the signal averaging. In the last several years, we aimed to expand the ^{19}F-MRI toolbox with tools that were not accessible at the time. This includes the introduction of inorganic fluoride-based nanocrystals (namely nanofluorides) and the ability to detect very low levels of targets with ^{19}F-MRI (through the implementation of the chemical exchange saturation transfer—the CEST strategy—into the ^{19}F-MRI framework) as summarized in Table 1.

This Feature Article summarizes our recent contributions in the field of ^{19}F-MRI, emphasizing the aim to expand the currently available ^{19}F-MRI toolbox with capabilities that were thus far applicable for molecular probes developed for ^{1}H-MRI. We describe the array of ^{19}F formulations developed in our lab, such as ultrasmall inorganic nanofluorides, fluorinated ligands, and host–guest supramolecular pairs. We also discuss how the principles of the CEST methodology can be implemented for

Table 1 Summary of the discussed techniques

	Detection principle	Applications	Merits	Limitations	Ref.
Nanofluorides	^{19}F-UTE	Mapping inflammation Mapping neuroinflammation "Multicolor" MRI	Very small ^{19}F-nanoformulations Established nanocrystals chemistry Straightforward surface modification Wide range of chemical shifts	Very short T_2 Broad linewidths	44, 51–53
iCEST	^{19}F-CEST	Mapping metal ions	Using ^{19}F-ligands with very low ion affinity Detection of low ion concentrations (µM range) Highly specific (frequency specificity)	Detecting ^{19}F-MR signal reduction (saturation transfer)	73–76
GEST	^{19}F-CEST	"Multicolor" MRI Mapping low concentrations of targets (µM level)	Amplifying ^{19}F-MR signals of targets (µM range) Using anesthetics as ^{19}F-MR agents Wide range of chemical shifts (paraGEST)	Detecting ^{19}F-MR signal reduction (saturation transfer) Requires the delivery of both the host and the guest entities to the region of interest	77–79, 83, 84

^{19}F-MRI studies by exemplifying this with different molecular architectures.

Nanofluorides for ^{19}F-MRI

Inorganic nanocrystals (NCs) have been extensively studied in biomedical research for decades. Their well-defined and adjustable properties (size, colloidal stability, *etc.*),[40,41] controlled inorganic content composition,[42] and their surface modifiability[43] are just a few examples of the attractiveness of inorganic NCs for diverse needs. Despite their obvious advantages and the ability to load a large fluoride content into their cores, inorganic NCs were not used in ^{19}F-MRI studies until very recently. More surprisingly, and probably due to the restricted mobility of the elements (*i.e.*, fluoride content) in their crystalline core, such NCs were not studied with liquid-state high-resolution ^{19}F-NMR.

In 2018, our group synthesized water-soluble and MR-trackable nanofluorides (NFs) for the first time.[44] Due to their very small size (~5 nm, Fig. 1a and b), the homonuclear dipolar interactions expected in solids, and thus in NFs, were found to be averaged out, allowing their detection by liquid-state ^{19}F-NMR. The first type of NFs, *i.e.*, citrate-coated CaF_2 NFs, show a single and stable ^{19}F-NMR peak while being dispersed in water (Fig. 1d). This singlet ^{19}F-NMR peak is expected for materials with a magnetically equivalent ^{19}F content. Indeed, the X-ray diffraction (XRD) pattern of CaF_2 NFs features a typical cubic-phase, fluorite-type, face-centered cubic (fcc) structure, as reflected by the first coordination sphere scheme (Fig. 1c). Thus, all fluorides in CaF_2 NFs have an identical position in a cell unit, which is manifested by a singlet ^{19}F-NMR peak. Note here that other NF formulations, LaF_3 NFs, for example, even synthesized as very small NCs and dispersed in solutions, did not give rise to a singlet and sharp

^{19}F-NMR peak as their fluoride content is distributed between different, not-magnetically equivalent positions in their crystal.

For subsequent biological applications, CaF_2 NFs were coated with polyethylene glycol (PEG) to improve their biocompatibility and enhance their retention time *in vivo*. To demonstrate that their ^{19}F-MR signal is preserved in a complex system and to examine their ^{19}F-MRI signal *in vivo*, PEG-coated CaF_2 NFs were injected into the inflamed footpads of mice. As shown in Fig. 1e, a clear ^{19}F-MR signal could be detected at the injection site, as well as in the region of draining lymph nodes one hour after injection, away from the location at which the NFs were introduced. Such an observation is in good agreement with the accumulation of imaging NCs of similar size[45] in the lymph nodes after their uptake by macrophages. These results proved that our proposed NFs are suitable nanoformulations for *in vivo* ^{19}F-MR visualization of biological events, such as inflammation.

Nanofluorides with enhanced relaxation properties

Increasing the sensitivity of ^{19}F-MRI is of paramount interest, as the concentrations of ^{19}F-entities at a given voxel of an MR image are limited. Several strategies have been developed toward this goal, such as: (i) increasing the number of ^{19}F atoms for a given imaging agent by synthesizing highly-fluorinated agents when possible;[31,46] (ii) shortening the T_1 relaxation of the fluorine-19 content to allow an increased number of signal averages at a given scan time;[47,48] or (iii) the use of special techniques, such as hyperpolarized ^{19}F-MRI.[49] The use of highly dense materials, such as NFs (3.18 g mL^{-1} for CaF_2),[44] results in the maximization of the ^{19}F-spins/volume possible and exceeds that obtained by organofluorines. Nevertheless, the relatively long T_1 of the fluoride content in NF, which is generally 10–15 s for NCs at the 5–10 nm size, limits the use of signal averaging to increase
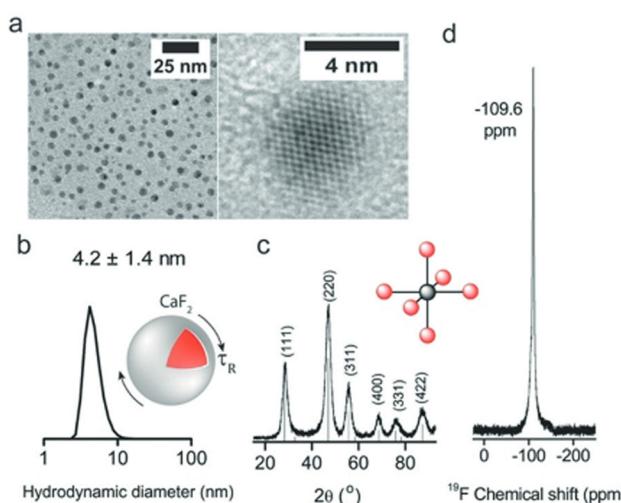
Fig. 1 ^{19}F-NMR and ^{19}F-MRI of water-soluble CaF_2 NFs. (a) TEM images and (b) size distribution measured by DLS. (c) XRD pattern with a schematic of the Ca^{2+} first coordination sphere. (d) High-resolution ^{19}F-NMR in water. (e) *In vivo* imaging of PEGylated CaF_2 showing anatomical [1]H-MRI for two representative mice (left) and matched ^{19}F-MRI (middle) shown as pseudo-color maps overlaid on [1]H-MRI (right). Modified with permission from ref. 44.

the signal-to-noise ratio (SNR) of the ^{19}F-MRI data, as this may require unreasonably long experiment times.

Paramagnetic relaxation enhancement (PRE)

Indeed, the applicability of NFs for dynamic studies is restricted due to their relatively long relaxation times (>10 s), which require long scan times to obtain robust ^{19}F-MRI data. One possible solution to this obstacle could be the introduction of paramagnetic relaxation enhancement (PRE), in which paramagnetic elements are incorporated into the crystal of NFs (Fig. 2a). The unpaired electrons of paramagnetic metal ions, for example, induce a PRE effect to the neighboring nuclear spins, such as those of fluorides in NFs, which results in shorter relaxation times (both T_1 and T_2). In this regard, as shortening of T_1 is desirable, drastic shortening of the T_2 of the neighboring fluorides may result in "blind spheres"[50] and the elimination of ^{19}F-NMR signals. Therefore, both the type of the introduced paramagnetic element and its amount should be carefully considered when preparing paramagnetic NFs with a short T_1. For example, we have shown that doping CaF$_2$ NFs with different paramagnetic elements (i.e., Sm^{3+}, Ce^{3+}, and Gd^{3+}) leads to a ^{19}F-NMR line-broadening that is dependent on the PRE capabilities of the dopant, with the most severe effect obtained, as expected, for Gd^{3+} (Fig. 2b). When Sm^{3+} ions (the lanthanide ion with lower PRE capabilities) were introduced to the crystal of CaF$_2$ NFs to obtain Sm:CaF$_2$, a 200-fold shortening of the T_1 of the fluorides was obtained (Fig. 2c).[51] The resultant ultrashort T_1 relaxation time of 70 ms led to an eight-fold enhancement of the ^{19}F-MR signal at a given scan time when compared to that obtained with undoped CaF$_2$ or those NFs doped with a diamagnetic lanthanide, La^{3+} (Fig. 2d and e).

Nanocrystalline defects relaxation enhancement (NDRE)

PRE effects induced by paramagnetic elements, although very efficient and widely used, have raised concerns about lanthanide biocompatibility and the difficulty of precise quantification of ^{19}F-MR signals due to line-broadening and "blind-spheres" induction. Inspired by the ability to control the pathway through which CaF$_2$ NFs are formed and identifying the linkage between different growth pathways and the crystal structure of CaF$_2$ formulations,[52] we proposed an alternative to PRE. This approach is based on the synthetic induction of crystallographic defects in NFs using phosphate-headed capping ligands that replaced the carboxylate-headed ligands used in previous studies. To shorten the T_1 of the fluorides in CaF$_2$ without the aid of paramagnetic elements, NFs were synthesized with oleyl phosphate (OP) as the capping ligand rather than with oleic acid (OA) to obtain either OP-CaF$_2$ or OA-CaF$_2$, respectively. High-resolution TEM of the two types of NFs (Fig. 3a and b) revealed a pronounced difference in the crystal architecture of NFs, with OA-CaF$_2$ exhibiting a well-ordered, highly crystalline lattice, while OP-CaF$_2$ crystals showed crystal defects at the type of grain boundaries (Fig. 3a). Importantly,


Fig. 2 Paramagnetically doped nanofluorides. (a) Schematic representation of the synthetic route for CaF$_2$ coated with oleic acid (OA) and doped with a lanthanide (Ln^{3+}). (b) ^{19}F-NMR spectra of OA-Ln:CaF$_2$ NCs with different Ln^{3+} dopants. All ^{19}F-NMR peaks resonate at $\delta = -109$ ppm. (c) T_1 values of Sm:CaF$_2$, La:CaF$_2$, and CaF$_2$ NCs. (d) ^{19}F-MRI of phantoms composed of La:CaF$_2$, Sm:CaF$_2$, and CaF$_2$ (70 mM of ^{19}F per sample) dispersed in water. (e) ^{19}F-MRI signal-to-noise ratios (SNRs) of the studied solutions shown in (d). Modified with permission from ref. 51.

Fig. 3 NDRE enhancement of the ^{19}F-MRI signal. Chemical structures and the corresponding HR-TEM images (scale bar 10 nm, in inset 5 nm) of (a) OA-CaF$_2$ and (b) OP-CaF$_2$ NCs. (c) T_1 relaxation times of OA- and OP-modified CaF$_2$. (d) In vivo ^{19}F-MRI of injected crystalline OA-CaF$_2$ (left leg, blue arrow) and defective OP-CaF$_2$ NCs (right leg, pink arrow). ^{19}F-MRI shown as a pseudo-color map overlaid on the anatomical ^{1}H-MR image of a live mouse. Modified with permission from ref. 53.

both types of NCs exhibited similar ^{19}F-NMR spectra with identical chemical shifts (-109 ppm) and comparable line widths. Interestingly, the T_1 value of the fluorides in OP-CaF$_2$ was found to be 10 times shorter (1 s) compared to that of the fluorides in OA-CaF$_2$ (11 s, Fig. 3c). This difference allows a dramatic shortening of the repetition time (TR) of ^{19}F-MRI acquisitions, essentially leading to an increase in the number of signal averages for a given scan time. The resultant four-fold improvement in the SNR of ^{19}F-MRI data demonstrated that the introduced crystallographic defects make the obtained NFs sensitive paramagnetic-free nanoprobes for ^{19}F-MR detection, even *in vivo* (Fig. 3d). This finding, which we termed nano-crystalline-defect relaxation enhancement (NDRE),[53] should be further explored to study other types of defects in NCs,[54] beyond the so-called grain boundaries obtained for OP-CaF$_2$.

Targeted nanofluorides

In addition to improving the relaxation and imaging properties of NFs, we have engineered their surface to grant them new properties and thus make them suitable for a wider range of biological functions. For example, we fabricated nanofluorides with a phospholipid coating to obtain a tunable platform for noninvasive MRI mapping of specific biological events. As a demonstration, we designed immune-cell-targeted NFs, which display sugar-functionalized phospholipids for enhanced recognition and receptors.[55,56] For this purpose, we modified the surface of paramagnetic Sm:CaF$_2$ NFs with lactose entities to obtain paramagnetic glyconanofluorides, and applied them to visualize neuroinflammatory activity in the central nervous system (CNS) following ischemic stroke.[51] The synthetic glyconanofluorides were preferentially taken up by activated immune cells when compared to non-modified nanofluorides (Fig. 4a and b) and accumulated in a stroke region that corresponded to the presence of immune cells, as shown by the ^{19}F-MR signal (Fig. 4d–f). Our demonstration of enhanced immune targetability in a clinically relevant model of neuropathology opens new routes for other biological targets and applications of nanofluorides in medicine.

Multiplexed visualization of nanocrystals

The heterogeneity of molecular signatures in pathological diseases mandates a method capable of identifying spatial and temporal fingerprints of these processes simultaneously. ^{19}F-MRI is an attractive technique for this, as two or more fluorine-containing probes can be imaged at the same time using the same approach and device. If the different probes contain a ^{19}F-entity that is surrounded by different chemical environments, they will be manifested by different ^{19}F-NMR chemical shifts, and thus, be monitored simultaneously, allowing for multiplexed analysis and a multicolor display.[12,57,58] To demonstrate the multiplex imaging capabilities of NFs, two different formulations, consisting of different cations (CaF$_2$ *vs.* SrF$_2$) were examined. Specifically, the NFs consisting of CaF$_2$ cores and those consisting of SrF$_2$ cores showed characteristic ^{19}F-NMR peaks resonating at -109 ppm and -88 ppm, respectively.
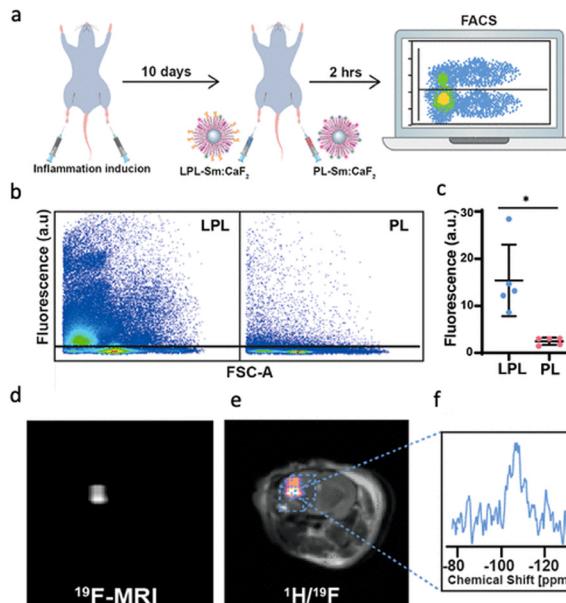
Fig. 4 Immunotargeting of glyconanofluorides *in vivo*. (a) Schematic illustration of the *in vivo* experimental setup used for the injection of both PL-Sm:CaF$_2$ (nanofluorides, *i.e.*, PL) or LPL-Sm:CaF$_2$ (glyconanofluorides, *i.e.*, LPL) NCs into inflamed mice footpads (20 μL of 25 mg mL^{-1} NCs). (b) Representative dot blots of FACS analysis of cells excised from lymph nodes 2 h post-injection of LPL-Sm:CaF$_2$ or PL-Sm:CaF$_2$ NCs. (c) Quantitative analysis of the FACS data (rhodamine) obtained from five different mice ($N = 5$, Student's t-test, * represents a p value <0.05). (d) *In vivo* ^{19}F-MRI and (e) ^{1}H/^{19}F-MRI overlay of a representative mouse 14 days after stroke induction. (f) Localized ^{19}F-NMR spectrum acquired from the area of the ischemic lesion (marked by a dashed-lined box). Modified with permission from ref. 51.

To demonstrate the multiplex imaging capabilities, the CaF$_2$ formulation was decorated with lactose-modified phospholipids (LPL-Sm:CaF$_2$) to obtain glyconanofluorides for immune cell targetability (as shown in Fig. 4). In contrast, SrF$_2$ formulations were decorated with unmodified phospholipids (PL-Sm:SrF$_2$) and used as control formulations that were not recognized by activated immune cells. Targeted and non-targeted NFs were injected as a mixture into a mouse footpad following inflammation induction (Fig. 5a–c). After the injection, the targeted glyconanofluorides (LPL-Sm:CaF$_2$, shown as the light blue ^{19}F-MRI signal in Fig. 5d–f) were found at significantly higher levels in the closer lymph node (LN). The two-fold higher ^{19}F-MRI signal of the targeted LPL-Sm:CaF$_2$ demonstrates the ability to spatially map the targetability of nanofluorides and present them in an artificial color MRI display. Importantly, the targeting moiety can be easily replaced to monitor additional biological events of interest in the future.

^{19}F-MR CEST

Developed in the 1960s,[59] the chemical exchange saturation transfer (CEST) NMR approach was "rediscovered" in the early 2000s when proposed as a contrast mechanism for MRI.[60]
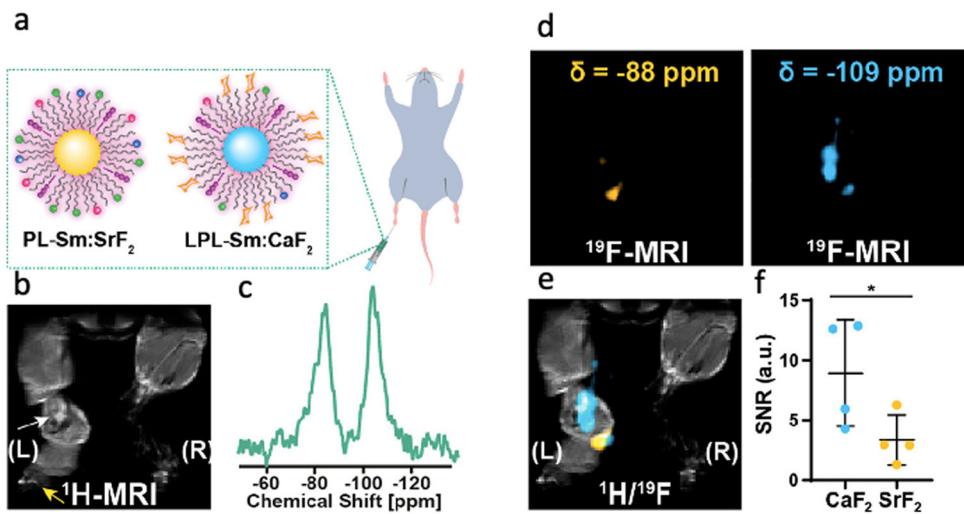
Fig. 5 Multiplexed visualization of immunotargeting by nanofluorides. (a) Schematic representation of nonglycosylated PL-Sm:SrF$_2$ and glycosylated LPL-Sm:CaF$_2$ NFs injected as a mixture to the inflamed footpad of a mouse. (b) ^{1}H-MRI of the inflamed footpad; the white arrow indicates the inflamed LN, and the yellow arrow represents the injection site. (c) *In vivo* ^{19}F-NMR spectrum acquired from the whole volume of the RF coil averaging all of the ^{19}F-NMR signals of the administered material (total injected PL-Sm:SrF$_2$ and LPL-Sm:CaF$_2$). (d) ^{19}F-MRI acquired with the center of frequency offset set at either -88 ppm (left, yellow) or -109 ppm (right, light blue). (e) Representative ^{1}H/^{19}F-MRI showing the higher accumulation of LPL-Sm:CaF$_2$ NCs in the LN. (f) Dot graph presenting the ^{19}F-MRI signal of either PL-Sm:SrF$_2$ or LPL-Sm:CaF$_2$ in the LN ROI ($N = 4$, Student's t-test, * represents a p value < 0.05). Modified with permission from ref. 51.

Currently, diamagnetic CEST (diaCEST) agents are frequently used in molecular and cellular MR imaging and cover a wide range of applications.[61–65] In CEST-MRI, a contrast is generated by the transfer of (saturated) magnetization from an exchangeable proton (of a solute, or a contrast agent) to that of water protons. Capitalizing on relatively fast exchange rates between exchangeable protons of the solute with water, even low-concentrated CEST agents ($\sim$mM concentration) can be detected *via* changes in surrounding water magnetization ($\sim$110 M of ^{1}H). The proton transfer ratio (PTR), which is manifested by magnetization transfer asymmetry (MTR$_{asym}$) or the CEST contrast can be simplified through eqn (1):[66]

$$\text{PTR} = x_s \cdot \alpha \cdot k_{sw} \cdot T_{1w}(1 - e^{-t_{sat}/T_{1w}}), \qquad (1)$$

where α is the saturation efficiency, k_{sw} is the exchange rate (frequently termed k_{ex}), T_{1w} is the T_1 of water, t_{sat} is the saturation time, and x_s is the ratio between the concentration of the exchangeable and the water protons as shown in eqn (2):

$$x_s = \frac{[\text{exchangable proton}]}{[\text{water proton}]}. \qquad (2)$$

Therefore, PTR, or the CEST effect, is enhanced, among other parameters (*e.g.*, k_{ex} and T_1) with an increase in the molar ratio x_s. This means that, with a given high and fixed concentration of water protons (110 M), CEST cannot be used for the detection of extremely low concentrations of targets that are frequently relevant to biological systems. Although this limitation may be overcome, to some extent, using CEST agents that experience very fast k_{ex}, as in some lanthanide complexes,[67,68] other strategies should be further proposed to benefit from this attractive and diverse contrast mechanism. With the goal to extend CEST MRI to detect a biological target that would be

expected at μM concentrations, we proposed the ^{19}F-CEST approach. In ^{19}F-CEST, the x_s ratio shown in eqn (1) represents the molar ratio between two exchanging pools of fluorine-19-containing materials. By reducing the concentrations of the bulk fluorinated agent (analogously to H$_2$O in ^{1}H-CEST) to a ^{19}F-MRI detectable concentration ($\sim$mM), much lower concentrations (μM) of the exchanging pool of the ^{19}F-element can be detected.

The establishment of ^{19}F-CEST opened a new avenue for the design of MRI sensors, since it exploits the benefits of both methodologies, *i.e.*, (i) the amplification effect of the CEST mechanism, and, because of the use of heteronuclear spins; (ii) the large $\Delta\omega$ (several hundreds of ppm for non-proton spins); (iii) the high sensitivity of the obtained $\Delta\omega$ to the local environment; and (iv) the lack of the background signal.

Metal-ion sensing using ^{19}F-CEST

In recent years, MRI has emerged as a method capable of mapping metal ions, with a distinct advantage over fluorescent-based methods in that it is able to provide spatial localization of the ions of interest in deep tissues. Paramagnetic "smart contrast agents" were designed to sense a range of metal ions with biological importance, with some exciting demonstrations for *in vivo* mapping of dynamic changes in the levels of labile Zn^{2+}[69,70] and Ca^{2+}[71,72] after pathological or physiological stimuli. We had extended the arsenal of such MRI smart agents with those that are based on fluorinated ligands capable of reversibly binding metal ions to generate ^{19}F-CEST contrast (or ion CEST, iCEST).[73]

With the proposal of iCEST,[73] we first showed that a combination of ^{19}F-MRI and CEST can be used to spatially monitor Ca^{2+} ions with high specificity, capitalizing on the dynamic exchange between the ion-bound and -free ^{19}F-ligand,
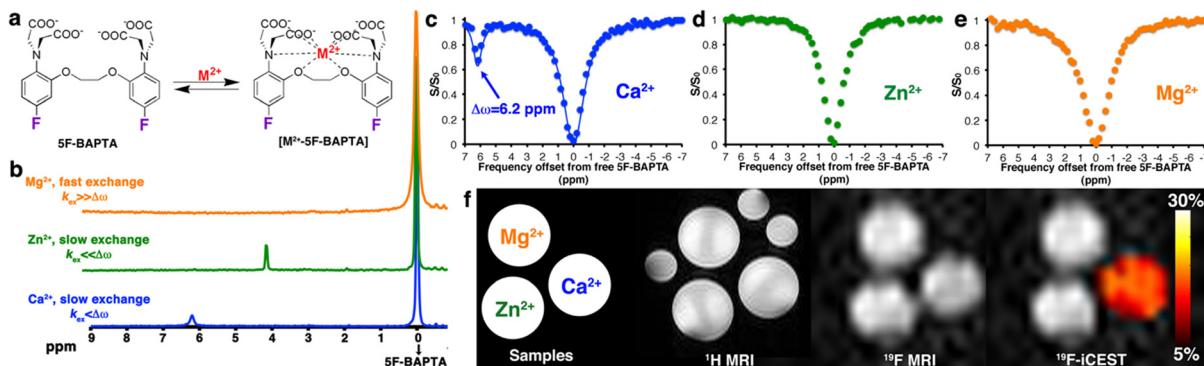
Fig. 6 The iCEST approach. (a) The dynamic exchange process between free 5F-BAPTA and M^{2+}-bound [M^{2+}-5F-BAPTA]. (b) ^{19}F NMR spectra of 5F-BAPTA in the presence of Mg^{2+}, Zn^{2+}, or Ca^{2+}. (c–e) Shown are ^{19}F-iCEST Z-spectra of solutions containing 10 mM 5F-BAPTA and 50 μM M^{2+}. (f) ^{1}H-MRI, ^{19}F-MRI, and iCEST ($\Delta\omega$ = 6.2) of M^{2+} solutions. Reproduced with permission from ref. 73.

and the shift in the $\Delta\omega$ value of ^{19}F in ^{19}F-NMR upon ion binding (Fig. 6). Specifically, upon binding of the fluorinated ligand 1,2-bis(*o*-aminophenoxy)ethane-*N*,*N*,*N'*,*N'*-tetraacetic acid (5F-BAPTA) to Ca^{2+}, a $\Delta\omega$ value of 6.2 ppm between the chemical shifts of free 5F-BAPTA and of the complex Ca^{2+}-5F-BAPTA was obtained in the ^{19}F-NMR spectrum. Since these two states of 5F-BAPTA are in a dynamic exchange, the ^{19}F-NMR signal of the Ca^{2+}-5F-BAPTA complex can be transferred to that of free 5F-BAPTA through saturation transfer, and thus, indirectly detect low Ca^{2+} concentrations. Importantly, competitive ions, such as Mg^{2+} or Zn^{2+}, which either do not bind (Mg^{2+}) or bind very strongly (Zn^{2+}) to 5F-BAPTA (Fig. 6b), cannot be detected with iCEST, making this approach highly specific (Fig. 6c–f). Using the tetrafluorinated derivative of the BAPTA (TF-BAPTA) chelate, a ^{19}F-probe for iCEST with enhanced specificity for Zn^{2+} and Fe^{2+} ions was obtained.[74]

Using TF-BAPTA as an iCEST MRI sensor for Zn^{2+}, an MRI-based strategy was developed for the detection of prostate cancer.[75] In that study, the authors showed that iCEST MRI is able to differentiate between normal and malignant prostate cells with a several-fold difference in the iCEST effect following

glucose-stimulated zinc secretion both *in vitro* and *in vivo*. The iCEST effect of TF-BAPTA decreased dramatically following the transition of normal prostate epithelial cells to cancer cells, showing the potential of this approach for the early diagnosis of prostate cancer in the future, before the appearance of commonly detected physiological and morphological changes.

However, this demonstration of the tight binding of Zn^{2+} to TF-BAPTA (K_d in the nM range) may deviate from the basal cationic levels at high concentrations of the ligand, which are required for ^{19}F-MRI. In addition, the relatively slow ion-chelate dissociation rate ($k_{off} = k_{ex} \sim 20$ s^{-1}) leads to a low iCEST contrast. To overcome these limitations, we rationalized a new fluorinated ligand for iCEST studies of labile Zn^{2+}, as shown in Fig. 7a. This ^{19}F-probe aimed to loosen the binding of Zn^{2+} through the elongation of the distance between the two pyridine rings of the binding entity to obtain a very weak ion-chelate affinity ($K_d = 5.5 \pm 0.5 \times 10^{-3}$ M) and a very fast dissociation rate ($k_{off} = 845 \pm 35$ s^{-1}).[76] Benefitting from the fast k_{off} for MRI signal amplification (through the CEST principles), we were able to detect a wide range of cation concentrations (0.5–50 μM) using a single imaging probe.
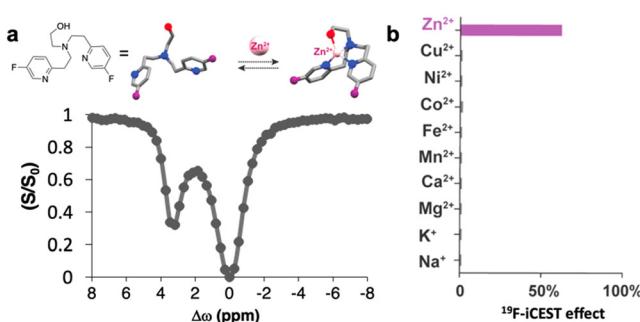

Fig. 7 ^{19}F-iCEST for mapping labile Zn^{2+} pools. (a) The molecular structure of the ultimate ^{19}F-iCEST probe designed for mapping labile Zn^{2+} and the obtained ^{19}F-iCEST effect ($\Delta\omega$ = 3.2 ppm) of 3 mM probe and 30 μM Zn^{2+}. (b) ^{19}F-iCEST effect ($\Delta\omega$ = 3.2 ppm) of 3 mM probe and 30 μM s-block (Na^+, K^+, Mg^{2+}, Ca^{2+}) and d-block (Mn^{2+}, Fe^{2+}, Co^{2+}, Ni^{2+}, Cu^{2+}, Zn^{2+}) metal ions obtained at 37 °C using a 9.4 T NMR spectrometer. (c) *In vivo* ^{19}F-iCEST maps of labile Zn^{2+} pools in the mouse brain. The results are shown for two regions of the brain: CA3 in the hippocampus (zinc-rich ROI, upper row) or the thalamus (TH, zinc-poor ROI, lower row). From left to right are the schematic illustrations of the setup used to deliver a zinc-responsive probe to either CA3 or TH, ^{1}H-MRI, ^{19}F-MRI obtained with saturation pulse applied "off-resonance" ($\Delta\omega$ = −3.2 ppm), ^{19}F-MRI obtained with saturation pulse applied "on resonance" ($\Delta\omega$ = +3.2 ppm), the ^{19}F-iCEST map (Zn^{2+} map) obtained from subtracting ^{19}F-MRI $S^{+3.2\ ppm}$ from ^{19}F-MRI $S^{-3.2\ ppm}$ overlaid on the ^{1}H-MRI. Modified with permission from ref. 76.
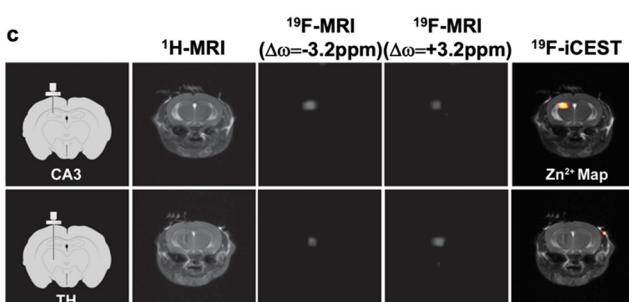
Relying on the chemical-shift specificity of NMR (Δw = +3.2 ppm), we demonstrated the frequency-specificity of the approach to exclusively map Zn^{2+}, compared to competitive cations (Fig. 7b).

This ultimate ^{19}F-iCEST probe was used for *in vivo* mapping of labile Zn^{2+} pools. For this purpose, two different regions of the brain, which are known for their different endogenous labile Zn^{2+} levels, were targeted. The CA3 region of the hippocampus was chosen as a region of interest (ROI) that is rich with labile Zn^{2+}, and the thalamus (TH) as an ROI with very low levels of labile Zn^{2+}. The ^{19}F-iCEST maps were derived following the delivery of the probe to the ROI and showed a significant ^{19}F-iCEST effect only in the CA3 region (Fig. 7c). When the very same probe was delivered at the same concentrations to a region that was not expected to have high levels of labile Zn^{2+} (TH), no ^{19}F-iCEST was observed. This approach should be further extended for the monitoring of dynamic changes in Zn^{2+} levels upon chemical or physiological stimulation to underline the role of this ion in appropriate brain function and brain-related diseases. Nevertheless, the fast washout of ^{19}F-iCEST from the imaging region and the need for its continuous infusion throughout the imaging session mandates additional development. One solution could be the use of smart imaging agents that self-assemble into large architectures under physiological conditions.[33] Using this strategy, we demonstrated a prolonged ^{19}F-MRI signal of an injectable probe even 20 hours after its delivery without the need for continuous infusion. These principles can be generalized and implemented for other types of imaging agents, which require prolonged imaging times or cannot tolerate fast washout rates.

^{19}F-guest exchange saturation transfer (^{19}F-GEST)

Capitalizing on the dynamic interactions in host–guest supramolecular assemblies and adopting the CEST principles, we proposed a novel approach termed GEST (guest exchange saturation transfer), which offers new possibilities for ^{19}F-MRI. In ^{19}F-GEST MRI, two pools of exchangeable fluorinated entities, A (free guest) and B (guest@host), experience different chemical shifts in the NMR spectrum (Fig. 8a). Similar to any CEST experiment, a pre-saturation pulse is applied at the frequency offset of pool B (set at a very low concentration, Fig. 8b), followed by a saturation transfer to reduce the ^{19}F-MRI signal of pool A (set at a relatively high and ^{19}F-MRI-detectable concentration, Fig. 8b). If the exchange process between A and B is fast enough, a significant change in the intensity of the ^{19}F-MRI signal of the fluorinated agent represented by pool A is detected, allowing the detection, indirectly, of very low concentrations of a bound guest represented as pool B.[77–79]

As mentioned above, the frequency encodability of ^{19}F-MRI agents had been used for the development of artificial MRI colors for multiplexed mapping of biological targets, mimicking the capabilities of multicolor luminescent probes.[12,57,80] Although they have a relatively large chemical shift range, which can span over 200 ppm, and can be further expanded using paramagnetic shift elements,[81,82] the need for their direct visualization in ^{19}F-MRI prevents their use for multiplexed
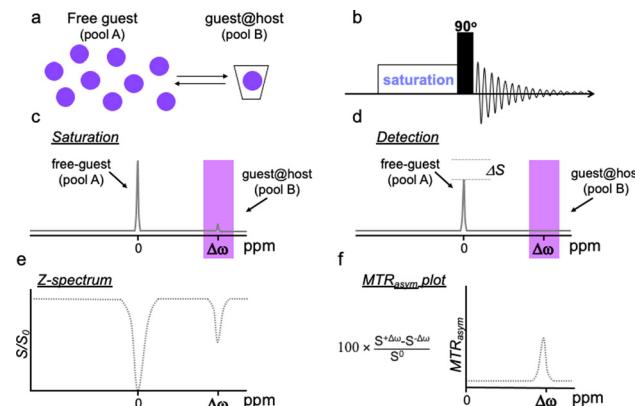
Fig. 8 Schematic illustration of GEST NMR principles. (a) A system containing a much higher concentration of the free guest (pool A) than that of the bound guest (guest@host complex, pool B) is studied. (b) A frequency-selective pre-saturation RF pulse is introduced prior to the excitation pulse in a 1D-NMR experiment. While the pre-saturation RF pulse (c, saturation) is applied at the frequency offset of the guest@host, a reduction in the signal of the free guest, ΔSI, is detected (d, detection). (e) The NMR signal intensity of the free guest (pool A) is plotted as a function of the frequency offset of the applied pre-saturation RF pulse, to obtain the z-spectrum (or CEST spectrum). (f) The MTR_{asym} plot calculated from the z-spectrum in (e). Reproduced with permission from ref. 79.

mapping of multiple targets at very low levels. In this regard, ^{19}F-GEST MRI may offer an alternative. Capitalizing on different chemical shifts of the complexed ^{19}F-guest (pool B) as a result of the properties of the molecular host, the GEST approach can be used for multi-target imaging with ^{19}F-MRI. This can be applied with diamagnetic molecular hosts based on the natural difference of their inner cavity properties[83] or with paramagnetic hosts, which are designed to induce a pseudo contact shift (PCS) to an exchanging ^{19}F-guest, in the same manner used by paramagnetic CEST agents.[84]

Diamagnetic ^{19}F-GEST

One major challenge in implementing GEST for ^{19}F-MRI studies is the need to deliver both the host and the ^{19}F-guest to the imaging region. To overcome this limitation, we took advantage of the natural properties of commonly used fluorinated anesthetics to be distributed in the brain through inhalation, thus providing a homogenous distribution of the ^{19}F-guest in the tissues.[83]

One specific fluorinated anesthetic, namely fluroxene (Fig. 9a), led to a pronounced ^{19}F-GEST contrast in the presence of two different molecular hosts, *i.e.*, cucurbit[7]uril (H_2) and octa-acid (H_7) with two opposite $\Delta\omega$ values, either downfield ($\Delta\omega$ = +1.6 ppm, represented as magenta in the GEST map), or upfield ($\Delta\omega$ = −2.2 ppm, represented as the green color of the GEST contrast) relative to the chemical shift of unbound fluroxene (Fig. 9b–e). Examining the ^{19}F-GEST effect in a localized spectroscopy manner showed the same observation (Fig. 9f and g). Here, two ^{19}F-NMR spectra were acquired followed by the subtraction of the ^{19}F-NMR spectrum obtained using the "on-resonance" pre-saturation pulse from that obtained when the pre-saturation pulse was applied "off-resonance."
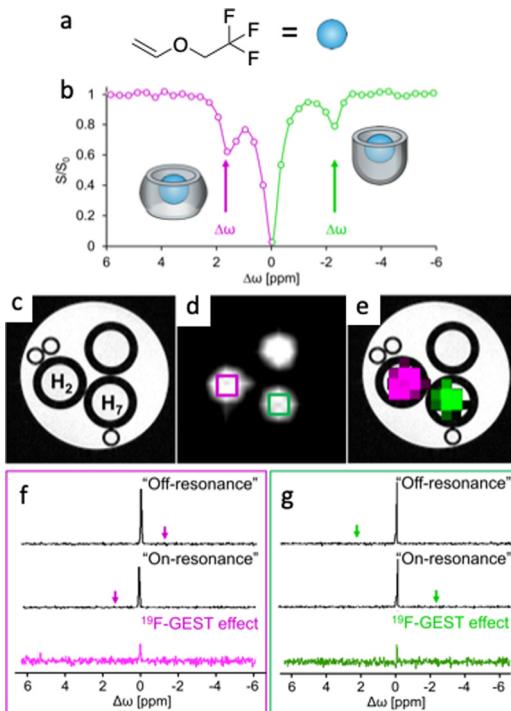
Fig. 9 Diamagnetic GEST: (a) the chemical structure of the fluorinated anesthetic fluroxene used as an inhalable ^{19}F-guest. (b) ^{19}F-GEST z-spectrum obtained from an aqueous solution containing a mixture of cucurbit[7]uril (H2) and dimeric octa acid (H7). The sample contained 5 mM fluroxene and 10 μM of each host. (c) ^{1}H-MRI, (d) ^{19}F-MRI, and (e) ^{19}F-GEST map of a three-tube phantom containing 5 mM fluroxene and 5 μM of either cucurbit[7]uril (H2) or octa acid (H7). A tube with 5 mM fluroxene only was used as a control. (f and g) Localized ^{19}F-GEST spectroscopy data of two voxels acquired from the tubes containing (f) H2:fluroxene (magenta) or (g) H7:fluroxene (green). The ^{19}F-GEST spectra represent the subtraction of the ^{19}F-NMR spectra obtained when the saturation pulse was applied "on-resonance" from the ^{19}F-NMR spectra obtained when the saturation pulse was applied "off-resonance." Data were acquired with a 9.4 T MRI scanner with B_1 = 2.5 μT/2 s. For fluroxene@H2, "on-resonance" was $\Delta\omega$ = +1.6 ppm and "off-resonance" was $\Delta\omega$ = −1.6 ppm. For fluroxene@H7, "on-resonance" was $\Delta\omega$ = −2.2 ppm and "off-resonance" was $\Delta\omega$ = +2.2 ppm. Modified with permission from ref. 83.

The obtained ^{19}F-GEST effect was clearly detected even in the presence of only 5 μM of either of the molecular hosts.[83]

Following the demonstration that a single fluorinated guest can be used to obtain two specific ^{19}F-GEST effects (Fig. 9), and to benefit from the fact that this guest can be used as an inhalable anesthetic, it was delivered to the mouse brain through inhalation using a dedicated system (Fig. 10a). The homogenous distribution of the inhaled ^{19}F-guest in the mouse brain was confirmed by ^{19}F-MRI (ultrashort TE-based scheme, Fig. 10d and e). The two different molecular hosts, either cucurbit[7]uril or octa acid, were delivered intracranially to two contralateral hemispheres of the examined mouse brain. Localized ^{19}F-GEST NMR data sets were acquired and clear in vivo ^{19}F-GEST effects were detected. These ^{19}F-GEST effects were obtained at opposite $\Delta\omega$ relative to that of the fluroxene (set at 0.0 ppm), i.e., downfield ($\Delta\omega$ = +1.6 ppm, Fig. 10f) for the H$_2$-fluroxene complex and upfield ($\Delta\omega$ = −2.2 ppm, Fig. 10g) for
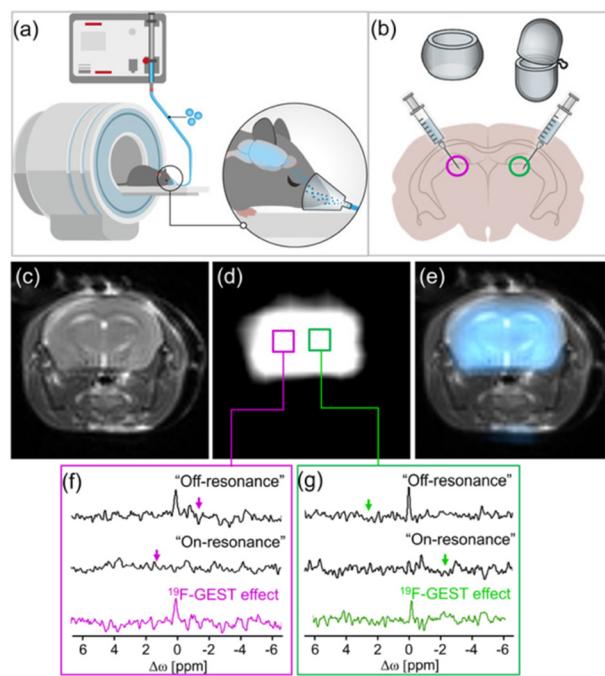
Fig. 10 In vivo ^{19}F-GEST of the anesthetic. (a and b) Schematic illustration of the in vivo experimental setup showing the delivery of the anesthetic to the mouse brain via inhalation (a) and the intracranial injection of the hosts (b). (c) ^{1}H-MRI, (d) UTE-^{19}F-MRI, and (e) ^{19}F-MRI signal overlaid on the ^{1}H-MRI of a live mouse anesthetized with 4% fluroxene. (f and g) Localized ^{19}F-GEST spectroscopy data of two voxels acquired from the regions injected with H2 (magenta) and (g) H7 (green). The ^{19}F-GEST spectra represent the subtraction of the ^{19}F-NMR spectra obtained when the saturation pulse was applied "on-resonance" from the ^{19}F-NMR spectra generated when the saturation pulse was applied "off-resonance." The "off-resonance" frequencies were $\Delta\omega$ = −1.6 ppm for H2-fluroxene and $\Delta\omega$ = +2.2 ppm for H7-fluroxene, and the "on-resonance" frequencies were $\Delta\omega$ = +1.6 ppm for H2-fluroxene and $\Delta\omega$ = −2.2 ppm for H7-fluroxene. Reproduced with permission from ref. 83.

the H$_7$-fluroxene complex. This demonstration provided a foundation for the development of novel molecular architectures detectable at low concentrations by ^{19}F-MRI. In future experiments, the molecular hosts for fluorine anesthetics can be modified in various ways. For example, molecular hosts can be fabricated to recognize and bind neuropathological features (e.g., brain tumors or amyloid plaques in Alzheimer's disease) and thus serve as highly-sensitive diagnostic tools for the detection of brain pathologies.

Paramagnetic GEST using paramagnetic cavitands

Despite the successful demonstration of ^{19}F-GEST in vivo[83] (Fig. 10), diamagnetic ^{19}F-GEST is limited to a relatively low spectral separation between a host-bound and -free fluorinated agent (Δw values of only a few ppm). This limitation restricts not just the ^{19}F-GEST spectral resolution and the ability to differentiate between different artificial ^{19}F-colors, but also the number of such colors that could be designed. Moreover, the $\Delta w > k_{ex}$ condition, which stands for ^{1}H-CEST, as well as for ^{19}F-GEST, mandates the use of host–guest molecular systems that experience relatively slow exchange dynamics.

To overcome these limitations, we adopted the principles of paramagnetic CEST agents[67,68] to introduce paramagnetic ^{19}F-GEST (paraGEST).[84] As a first step, we synthesized a library of paramagnetic α-cyclodextrins (para-CDs, Fig. 11a) as the putative paramagnetic hosts. Then, the essential structural characteristics of the ^{19}F-guest were studied, which necessitated a benzylamine backbone for paraGEST observation, with the position of the fluorine substituent affecting the observed Δw of the paraGEST effect.

Having established the paraGEST principles for a single host–guest pair, we used this approach for multiplexed ^{19}F-MR imaging based on paramagnetic supramolecular systems. We termed the generation of artificial colors for MR images the Color Display by Exploiting Host–guest Dynamics (CODE-HD), which was demonstrated by nine host–guest pairs. Using 4-(trifluoromethyl)benzylamine as the fluorinated guest (guest 2 at Fig. 11b) and different para-CDs, an array of single and well-defined paraGEST effects were obtained for all examined pairs. Each host–guest pair showed a characteristic $\Delta\omega$ value, which depends on the identity of the lanthanide (Tm, Er, Yb, Eu, Nd, Pr, Ho, Tb, or Dy) at the paraCD host (or Ln-CD). Assigning each $\Delta\omega$ value a color provided us with nine artificial paraGEST colors that could be displayed as an MRI map (Fig. 11b). In contrast to other luminescent colors and, even in relation to [1]H-CEST colors, the color palette of paraGEST can be easily converted to a different one by replacing the fluorinated guest. For example, using

3,5-difluorobenzylamine as the guest (guest 3) resulting in a different characteristic $\Delta\omega$ value with each of the paraCD hosts (Fig. 11c). Using a competitor (non-fluorinated) guest (guest 5, Fig. 11d), which bound to the paraCD host much more tightly, resulting in the elimination of the paraGEST effect (Fig. 11d), a unique feature that is not applicable for luminescence-based colors and may be considered in the future for advanced applications.

Summary and future perspectives

The growing interest in quantitative methods for *in vivo* imaging with a reduced level of false-positive results had led to the expansion of the available fluorinated probes for background-free molecular and cellular ^{19}F-MRI studies. Indeed, these demonstrations continue to stimulate the development of more advanced agents for improved performances and diverse capabilities that were not demonstrated in the field of ^{19}F-MRI just a few years ago. In that regard, our development summarized here expands the ^{19}F-MRI toolbox available today, not just with new molecular architectures, but also with novel concepts for future designs of fluorinated probes. The use of nanofluorides as imaging agents of ^{19}F-MRI offers to combine the advantages of ultrasmall inorganic NCs with the merits of background-free imaging, and thus, proposes an alternative to metal-oxide NCs.
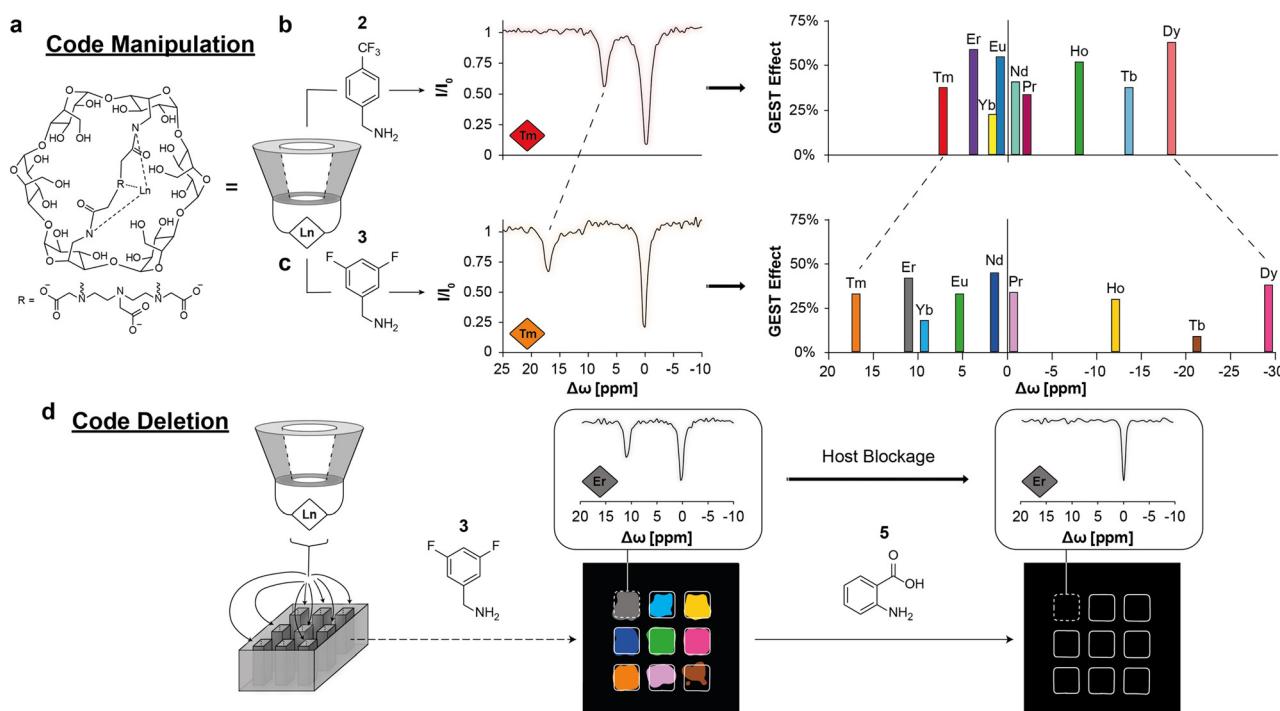

Fig. 11 The CODE-HD method based on paraGEST. (a) The molecular structure of the paramagnetic host Ln-CD. The principles for code manipulation are shown in (b) and (c). The obtained z-spectra of a solution of thulium-cyclodextrin (Tm-CD, red and orange diamonds) in the presence of either 2 (b) or 3 (c), and plots showing the obtained chemical shift offset ($\Delta\omega$) values from paraGEST experiments with different Ln-CDs as the hosts and either 2 (b) or 3 (c) as the guest, and the assigned colors for each host–guest pair. (d) Code deletion. CODE-HD color map obtained from different pairs of Ln-CD and 3, which is deleted upon anthranilic acid (5) addition to each one of the wells. The z-spectra obtained from the well containing erbium-cyclodextrin (Er-CD, gray diamond) before and after the addition of 5 is shown in the insets. Modified with permission from ref. 84.

For example, nanofluorides can be used to label and track extracellular vesicles (EVs), which garnered much interest recently in a variety of fields. The *ca.* 100–120 nm size of EVs requires their labeling with relatively small inorganic NCs, such as iron oxide NCs for MRI studies,[85,86] thus making nanofluorides very attractive for background-free MRI of EVs. The implementation of the CEST contrast mechanism for ^{19}F-MRI studies opens new opportunities to detect very low concentrations of the target that were otherwise undetectable. Shown for several metal ions, ^{19}F-iCEST probes should now be further developed for additional metal ions with biological relevance. ^{19}F-GEST MRI opens new directions through which multiple targets at very low concentrations could be monitored and mapped in a multicolor way.

The ^{19}F-MRI toolbox is continuously expanding with additional developments by others, beyond those summarized in this Feature Article. For example, the recent implementation of hyperpolarization techniques to amplify ^{19}F-MRI signals is very promising[49,87] in light of the revolution made by hyperpolarized ^{13}C-MRI.[88] Another example is the use of fluorinated ionic liquids, which were developed to undergo phase transition upon exposure to environmental stimulation, and which, therefore, could be used as "turn-on" ^{19}F-MRI-responsive agents.[27,80] The recent developments in hardware allow the use of cryogenic RF coils for improved SNRs of ^{19}F-MRI data,[89] and advanced acquisition schemes are being implemented to improve the performance of ^{19}F-MRI studies.[90,91] In light of these developments, the collaboration of MR physicists, chemists, radiologists, and scientists from other fields should be encouraged to advance ^{19}F-MRI to new frontiers that are as yet inaccessible to this background-free imaging approach.

Conflicts of interest

There are no conflicts to declare.

Acknowledgements

References

1 G. N. Holland, P. A. Bottomley and W. S. Hinshaw, *J. Magn. Reson.*, 1977, **28**, 133–136.
2 S. Mizukami, R. Takikawa, F. Sugihara, Y. Hori, H. Tochio, M. Wälchli, M. Shirakawa and K. Kikuchi, *J. Am. Chem. Soc.*, 2008, **130**, 794–795.
3 J.-X. Yu, V. D. Kodibagkar, R. R. Hallac, L. Liu and R. P. Mason, *Bioconjug. Chem.*, 2012, **23**, 596–603.
4 M. Yu, B. S. Bouley, D. Xie and E. L. Que, *Dalton Trans.*, 2019, **48**, 9337–9341.
5 K. Srivastava, E. A. Weitz, K. L. Peterson, M. Marjańska and V. C. Pierre, *Inorg. Chem.*, 2017, **56**, 1546–1557.
6 O. Sedlacek, D. Jirak, A. Galisova, E. Jager, J. E. Laaser, T. P. Lodge, P. Stepanek and M. Hruby, *Chem. Mater.*, 2018, **30**(15), 4892–4896.

7 C. Fu, S. Herbst, C. Zhang and A. K. Whittaker, *Polym. Chem.*, 2017, **8**, 4585–4595.
8 E. Ahrens, B. Helfer, C. F. O'Hanl and C. Schirda, *Magn. Reson. Med.*, 2014, **72**, 1696–1701.
9 E. Swider, A. H. J. Staal, N. van Riessen, L. Jacobs, P. B. White, R. Fokkink, G.-J. Janssen, E. van Dinther, C. G. Figdor, I. J. de Vries, O. Koshkina and M. Srinivas, *RSC Adv.*, 2018, **8**, 6460–6470.
10 M. Srinivas, P. A. Morel, L. A. Ernst, D. H. Laidlaw and E. T. Ahrens, *Magn. Reson. Med.*, 2007, **58**, 725–734.
11 A. Gálisová, V. Herynek, E. Swider, E. Sticová, A. Pátiková, L. Kosinová, J. Kříž, M. Hájek, M. Srinivas and D. Jirák, *Mol. Imaging Biol.*, 2019, **21**, 454–464.
12 U. Flögel, S. Temme, C. Jacoby, T. Oerther, P. Keul, V. Flocke, X. Wang, F. Bönner, F. Nienhaus, K. Peter, J. Schrader, M. Grandoch, M. Kelm and B. Levkau, *Nat. Commun.*, 2021, **12**, 5847.
13 E. T. Ahrens, R. Flores, H. Xu and P. A. Morel, *Nat. Biotechnol.*, 2005, **23**, 983–987.
14 U. Flögel, Z. Ding, H. Hardung, S. Jander, G. Reichmann, C. Jacoby, R. Schubert and J. Schrader, *Circulation*, 2008, **118**, 140–148.
15 P. Boehm-Sturm, L. Mengler, S. Wecker, M. Hoehn and T. Kallur, *PLoS One*, 2011, **6**, e29040.
16 T. Nakamura, F. Sugihara, H. Matsushita, Y. Yoshioka, S. Mizukami and K. Kikuchi, *Chem. Sci.*, 2015, **6**, 1986–1990.
17 J. Gaudet, E. Ribot, Y. Chen, K. Gilbert and P. Foster, *PLoS*, 2015, **10**, e0118544.
18 K. Cai, L. Zhang, J. Myerson, W. Huang, S. D. Caruthers, G. M. Lanza, S. A. Wickline and P. M. Winter, *J. Cardiovasc. Magn. Reson.*, 2009, **11**, T6.
19 X. Xu, Y. Yan, F. Liu, L. Wu, M. Shao, K. Wang, X. Sun, Y. Li, E. S. W. Beinpuo and B. Shen, *J. Magn. Reson. Imaging*, 2018, **48**, 1617–1625.
20 H. Zhang, Q. Yu, Y. Li, Z. Yang, X. Zhou, S. Chen and Z.-X. Jiang, *Chem. Commun.*, 2020, **56**, 3617–3620.
21 H. Zhang, S. Bo, K. Zeng, J. Wang, Y. Li, Z. Yang, X. Zhou, S. Chen and Z.-X. Jiang, *J. Mater. Chem. B*, 2020, **8**, 4469–4474.
22 T. Wu, K. Chen, M. Jiang, A. Li, X. Peng, S. Chen, Z. Yang, X. Zhou, X. Zheng and Z.-X. Jiang, *Org. Biomol. Chem.*, 2022, **20**, 1299–1305.
23 D. Xie, M. Yu, R. T. Kadakia and E. L. Que, *Acc. Chem. Res.*, 2020, **53**, 2–10.
24 M. Yu, D. Xie, R. T. Kadakia, W. Wang and E. L. Que, *Chem. Commun.*, 2020, **56**, 6257–6260.
25 D. Xie, T. L. King, A. Banerjee, V. Kohli and E. L. Que, *J. Am. Chem. Soc.*, 2016, **138**, 2937–2940.
26 A. Sarkar, I. E. Biton, M. Neeman and A. Datta, *Inorg. Chem. Commun.*, 2017, **78**, 21–24.
27 X. Zhu, X. Tang, H. Lin, S. Shi, H. Xiong, Q. Zhou, A. Li, Q. Wang, X. Chen and J. Gao, *Chem*, 2020, **6**, 1134–1148.
28 R. Zhang, Q. Ma, G. Hu and L. Wang, *Anal. Chem.*, 2022, **94**, 3727–3734.
29 A. Li, X. Luo, L. Li, D. Chen, X. Liu, Z. Yang, L. Yang, J. Gao and H. Lin, *Anal. Chem.*, 2021, **93**, 16552–16561.
30 X. Huang, G. Huang, S. Zhang, K. Sagiyama, O. Togao, X. Ma, Y. Wang, Y. Li, T. C. Soesbe, B. D. Sumer, M. Takahashi, A. D. Sherry and J. Gao, *Angew. Chem., Int. Ed.*, 2013, **52**, 8074–8078.
31 K. Wang, H. Peng, K. J. Thurecht, S. Puttick and A. K. Whittaker, *Polym. Chem.*, 2013, **4**, 4480–4489.
32 X. Tang, X. Gong, A. Li, H. Lin, C. Peng, X. Zhang, X. Chen and J. Gao, *Nano Lett.*, 2020, **20**, 363–371.
33 N. D. Tirukoti, L. Avram, R. Mashiach, H. Allouche-Arnon and A. Bar-Shir, *Chem. Commun.*, 2022, **58**, 11410–11413.
34 O. Sedlacek, D. Jirak, A. Galisova, E. Jager, J. E. Laaser, T. M. Lodge, P. Stepanek and M. Hruby, *Chem. Mater.*, 2018, **30**, 4892–4896.
35 J. Salaam, M. Minoshima and K. Kikuchi, *Anal. Sens.*, 2022, e202200081.
36 I. Tirotta, V. Dichiarante, C. Pigliacelli, G. Cavallo, G. Terraneo, F. B. Bombelli, P. Metrangolo and G. Resnati, *Chem. Rev.*, 2015, **115**, 1106–1129.
37 C. Zhang, K. Yan, C. Fu, H. Peng, C. J. Hawker and A. K. Whittaker, *Chem. Rev.*, 2022, **122**, 167–208.
38 M. H. Cho, S. H. Shin, S. H. Park, D. K. Kadayakkara, D. Kim and Y. Choi, *Bioconjug. Chem.*, 2019, **30**, 2502–2518.
39 S. Temme, F. Bönner, J. Schrader and U. Flögel, *Wiley Interdiscip. Rev.: Nanomed. Nanobiotechnol.*, 2012, **4**, 329–343.

40 J. Park, E. Lee, N.-M. Hwang, M. Kang, S. C. Kim, Y. Hwang, J.-G. Park, H.-J. Noh, J.-Y. Kim, J.-H. Park and T. Hyeon, *Angew. Chem., Int. Ed.*, 2005, **44**, 2872–2877.

41 Z. Zhao, Z. Zhou, J. Bao, Z. Wang, J. Hu, X. Chi, K. Ni, R. Wang, X. Chen, Z. Chen and J. Gao, *Nat. Commun.*, 2013, **4**, 2266.

42 J.-H. Lee, Y.-M. Huh, Y. Jun, J. Seo, J. Jang, H.-T. Song, S. Kim, E.-J. Cho, H.-G. Yoon, J.-S. Suh and J. Cheon, *Nat. Med.*, 2007, **13**, 95–99.

43 R. Weissleder, K. Kelly, E. Y. Sun, T. Shtatland and L. Josephson, *Nat. Biotechnol.*, 2005, **23**, 1418–1423.

44 I. Ashur, H. Allouche-Arnon and A. Bar-Shir, *Angew. Chem., Int. Ed.*, 2018, **57**, 7478–7482.

45 O. L. Gobbo, K. Sjaastad, M. W. Radomski, Y. Volkov and A. Prina-Mello, *Theranostics*, 2015, **5**, 1249–1263.

46 C. Chirizzi, C. Morasso, A. A. Caldarone, M. Tommasini, F. Corsi, L. Chaabane, R. Vanna, F. B. Bombelli and P. Metrangolo, *J. Am. Chem. Soc.*, 2021, **143**, 12253–12260.

47 M. Srinivas, A. Heerschap, E. T. Ahrens, C. G. Figdor and I. J. M. de Vries, *Trends Biotechnol.*, 2010, **28**, 363–370.

48 E. Matei and A. M. Gronenborn, *Angew. Chem., Int. Ed.*, 2016, **55**, 150–154.

49 J. Bernarding, F. Euchner, C. Bruns, R. Ringleb, D. Müller, T. Trantzschel, J. Bargon, U. Bommerich and M. Plaumann, *Chem. Phys. Chem.*, 2018, **19**, 2453–2456.

50 W. Li, Q. Zhang, J. J. Joos, P. F. Smet and J. Auf der Günne, *Phys. Chem. Chem. Phys.*, 2019, **21**, 10185–10194.

51 D. Cohen, R. Mashiach, L. Houben, A. Galisova, Y. Addadi, D. Kain, A. Lubart, P. Blinder, H. Allouche-Arnon and A. Bar-Shir, *ACS Nano*, 2021, **15**, 7563–7574.

52 R. Mashiach, H. Weissman, L. Avram, L. Houben, O. Brontvein, A. Lavie, V. Arunachalam, M. Leskes, B. Rybtchinski and A. Bar-Shir, *Nat. Commun.*, 2021, **12**, 229.

53 R. Mashiach, D. Cohen, L. Avram, T. Harris, I. Pinkas, L. Houben, H. Allouche-Arnon and A. Bar-Shir, *Nano Lett.*, 2020, **20**, 7207–7212.

54 R. Xu, F. Meng, Y. Liu, D. Duosiken, K. Sun, S. Pan and K. Tao, *Chem. Commun.*, 2021, **57**, 9148–9151.

55 J. L. Betker and T. J. Anchordoquy, *J. Pharm. Sci.*, 2020, **109**, 1573–1580.

56 M. Rabyk, A. Galisova, M. Jiratova, V. Patsula, L. Srbova, L. Loukotova, J. Parnica, D. Jirak, P. Stepanek and M. Hruby, *J. Mater. Chem. B*, 2018, **6**(17), 2584–2596.

57 K. Akazawa, F. Sugihara, T. Nakamura, H. Matsushita, H. Mukai, R. Akimoto, M. Minoshima, S. Mizukami and K. Kikuchi, *Angew. Chem., Int. Ed.*, 2018, **57**, 16742–16747.

58 C. Chirizzi, D. De Battista, I. Tirotta, P. Metrangolo, G. Comi, F. B. Bombelli and L. Chaabane, *Radiology*, 2019, **291**, 351–357.

59 S. Forsén, *J. Chem. Phys.*, 1963, **39**, 2892.

60 K. M. Ward, A. H. Aletras and R. S. Balaban, *J. Magn. Reson.*, 2000, **143**, 79–87.

61 A. Bar-Shir, J. W. M. Bulte and A. A. Gilad, *ACS Chem. Biol.*, 2015, **10**, 1160–1170.

62 K. W. Y. Chan, M. T. McMahon, Y. Kato, G. Liu, J. W. M. Bulte, Z. M. Bhujwalla, D. Artemov and P. C. M. van Zijl, *Magn. Reson. Med.*, 2012, **68**, 1764–1773.

63 Z. Han, Y. Li, J. Zhang, J. Liu, C. Chen, P. C. van Zijl and G. Liu, *Cancer Res.*, 2019, **79**, 2775–2783.

64 D. L. Longo, A. Busato, S. Lanzardo, F. Antico and S. Aime, *Magn. Reson. Med.*, 2013, **70**, 859–864.

65 H. Allouche-Arnon, O. Khersonsky, N. D. Tirukoti, Y. Peleg, O. Dym, S. Albeck, A. Brandis, T. Mehlman, L. Avram, T. Harris, N. N. Yadav, S. J. Fleishman and A. Bar-Shir, *Nat. Biotechnol.*, 2022, **40**, 1143–1149.

66 P. C. M. van Zijl and N. N. Yadav, *Magn. Reson. Med.*, 2011, **65**, 927–948.

67 S. Aime, D. Delli Castelli, F. Fedeli and E. Terreno, *J. Am. Chem. Soc.*, 2002, **124**, 9364–9365.

68 S. Zhang, R. Trokowski and A. D. Sherry, *J. Am. Chem. Soc.*, 2003, **125**, 15288–15289.

69 A. J. M. Lubag, L. M. De Leon-rodriguez, S. C. Burgess and A. D. Sherry, *Proc. Natl. Acad. Sci. U. S. A.*, 2011, **108**, 18400–18405.

70 V. Clavijo Jordan, C. D. G. Hines, L. T. Gantert, S. Wang, S. Conarello, C. Preihs, S. Chirayil, M. Klimas, J. L. Evelhoch and A. D. Sherry, *Front. Endocrinol.*, 2021, **12**, 641722.

71 T. Savić, G. Gambino, V. S. Bokharaie, H. R. Noori, N. K. Logothetis and G. Angelovski, *Proc. Natl. Acad. Sci. U. S. A.*, 2019, **116**, 20666–20671.

72 A. Barandov, B. B. Bartelle, C. G. Williamson, E. S. Loucks, S. J. Lippard and A. Jasanoff, *Nat. Commun.*, 2019, **10**, 897.

73 A. Bar-Shir, A. A. Gilad, K. W. Y. Chan, G. Liu, P. C. M. van Zijl, J. W. M. Bulte and M. T. McMahon, *J. Am. Chem. Soc.*, 2013, **135**, 12164–12167.

74 A. Bar-Shir, N. N. Yadav, A. A. Gilad, P. C. M. van Zijl, M. T. McMahon and J. W. M. Bulte, *J. Am. Chem. Soc.*, 2015, **137**, 78–81.

75 Y. Yuan, Z. Wei, C. Chu, J. Zhang, X. Song, P. Walczak and J. W. M. Bulte, *Angew. Chem., Int. Ed.*, 2019, **58**, 15512–15517.

76 N. D. Tirukoti, L. Avram, T. Haris, B. Lerner, Y. Diskin-Posner, H. Allouche-Arnon and A. Bar-Shir, *J. Am. Chem. Soc.*, 2021, **143**, 11751–11758.

77 L. Avram, A. D. Wishard, B. C. Gibb and A. Bar-Shir, *Angew. Chem., Int. Ed.*, 2017, **56**, 15314–15318.

78 L. Avram, M. A. Iron and A. Bar-Shir, *Chem. Sci.*, 2016, **7**, 6905–6909.

79 L. Avram and A. Bar-Shir, *Org. Chem. Front.*, 2019, **6**, 1503–1512.

80 X. Zhu, H. Xiong, S. Wang, Y. Li, J. Chi, X. Wang, T. Li, Q. Zhou, J. Gao and S. Shi, *Adv. Healthc. Mater.*, 2022, **11**, e2102079.

81 M. Yu, B. S. Bouley, D. Xie, J. S. Enriquez and E. L. Que, *J. Am. Chem. Soc.*, 2018, **140**, 10546–10552.

82 J. Kretschmer, T. David, M. Dračínský, O. Socha, D. Jirak, M. Vít, R. Jurok, M. Kuchař, I. Císařová and M. Polasek, *Nat. Commun.*, 2022, **13**, 3179.

83 R. Shusterman-Krush, N. D. Tirukoti, A. K. Bandela, L. Avram, H. Allouche-Arnon, X. Cai, B. C. Gibb and A. Bar-Shir, *Angew. Chem., Int. Ed.*, 2021, **60**, 15405–15411.

84 E. Goren, L. Avram and A. Bar-Shir, *Nat. Commun.*, 2021, **12**, 3072.

85 A. Galisova, J. Zahradnik, H. Allouche-Arnon, M. I. Morandi, P. Abou Karam, M. Fisler, O. Avinoam, N. Regev-Rudzki, G. Schreiber and A. Bar-Shir, *ACS Nano*, 2022, **16**, 12276–12289.

86 Z. Han, S. Liu, Y. Pei, Z. Ding, Y. Li, X. Wang, D. Zhan, S. Xia, T. Driedonks, K. Witwer, R. Weiss, P. Zijl, J. Bulte, L. Cheng and G. Liu, *J. Extracell. vesicles*, 2021, **10**, e12054.

87 J. Bernarding, C. Bruns, I. Prediger and M. Plaumann, *Appl. Magn. Reson.*, 2022, **53**, 1375–1398.

88 K. Golman, J. H. Ardenkjaer-Larsen, J. S. Petersson, S. Mansson and I. Leunbach, *Proc. Natl. Acad. Sci. U. S. A.*, 2003, **100**, 10435–10439.

89 S. Waiczies, J. M. Millward, L. Starke, P. R. Delgado, T. Huelnhagen, C. Prinz, D. Marek, D. Wecker, R. Wissmann, S. P. Koch, P. Boehm-Sturm, H. Waiczies, T. Niendorf and A. Pohlmann, *Sci. Rep.*, 2017, **7**, 9808.

90 L. Starke, A. Pohlmann, C. Prinz, T. Niendorf and S. Waiczies, *Magn. Reson. Med.*, 2020, **84**, 592–608.

91 J. Chen, P. Pal and E. T. Ahrens, *NMR Biomed.*, 2022, **35**, e4725.